Title
Radiative transport in the delta- approximation for semi-infinite turbid media

Journal
Medical Physics, 35(2)

ISSN
0094-2405

Authors
Seo, InSeok
Hayakawa, Carole K
Venugopalan, Vasan

Publication Date
2008-01-29

DOI
10.1118/1.2828184

Published in final edited form as:
Med Phys. 2008 February ; 35(2): 681–693.

Radiative transport in the delta-P_1 approximation for semi-infinite turbid media

InSeok Seo, **Carole K. Hayakawa**, and **Vasan Venugopalan**[a]
Department of Chemical Engineering and Materials Science, University of California, Irvine, Irvine, California 92697-2575 and Laser Microbeam and Medical Program, Beckman Laser Institute and Medical Clinic, 1002 Health Sciences Rd., University of California, Irvine, Irvine, California 92612-3010

Abstract

We have developed an analytic solution for spatially resolved diffuse reflectance within the δ-P_1 approximation to the radiative transport equation for a semi-infinite homogeneous turbid medium. We evaluate the performance of this solution by comparing its predictions with those provided by Monte Carlo simulations and the standard diffusion approximation. We demonstrate that the δ-P_1 approximation provides accurate estimates for spatially resolved diffuse reflectance in both low and high scattering media. We also develop a multi-stage nonlinear optimization algorithm in which the radiative transport estimates provided by the δ-P_1 approximation are used to recover the optical absorption (μ_a), reduced scattering (μ_s'), and single-scattering asymmetry coefficients (g_1) of liquid and solid phantoms from experimental measurements of spatially resolved diffuse reflectance. Specifically, the δ-P_1 approximation can be used to recover μ_a, μ_s', and g_1 with errors within ±22%, ±18%, and ±17%, respectively, for both intralipid-based and siloxane-based tissue phantoms. These phantoms span the optical property range $4<(\mu_s'/\mu_a)<117$. Using these same measurements, application of the standard diffusion approximation resulted in the recovery of μ_a and μ_s' with errors of ±29% and ±25%, respectively. Collectively, these results demonstrate that the δ-P_1 approximation provides accurate radiative transport estimates that can be used to determine accurately the optical properties of biological tissues, particularly in spectral regions where tissue may display moderate/low ratios of reduced scattering to absorption (μ_s'/μ_a).

I. INTRODUCTION

The radiative transport equation (RTE) provides the basis for particle-based radiative transport models. The RTE is an integro-differential equation that is amenable to complete analytic solution in only a small number of cases. Moreover, even though a Green's function for the RTE has been recently developed, the computational costs required for its evaluation, especially for large single-scattering asymmetry coefficients, are substantial.[1] These considerations have given rise to the prevalent use of the standard diffusion approximation (SDA) to provide an approximate solution to the RTE. The SDA has been a useful tool to investigate light transport within turbid media due to its simple analytic form and validity in highly scattering media. The SDA results from the substitution of first-order spherical harmonic (Legendre polynomial) expansions to approximate the radiance and phase function within the RTE. The use of these low-order expansions prevents the SDA from providing accurate radiative transport estimates at locations proximal to collimated sources and

[a]Author to whom correspondence should be addressed; vvenugop@uci.edu.

interfaces of significant refractive index mismatch, as well as in media where the reduced scattering coefficient (μ_s') is only moderately dominant over the absorption coefficient (μ_a) i.e., for $(\mu_s'/\mu_a) \lesssim 10–30$.[2–4] This means that for spatially resolved reflectance measurements made even in highly scattering media, predictions provided by the SDA are unreliable at source-detector (s-d) separations ρ comparable to a transport mean free path $l^*[=1/(\mu_a+\mu_s')]$. Practically, these limits restrict the use of the SDA to measurements made on biological tissues in the spectral range of λ = 650–1100 nm in which soft tissues typically possess $(\mu_s'/\mu_a) \gtrsim 10$.[5]

The development of improved radiative transport models that are amenable to rapid computation would enable the quantitative analysis of optical signals acquired outside the λ = 650–1100 nm spectral region as well as from superficial tissue volumes (e.g., epithelial tissues) using small s-d separations. Moreover, because light signals acquired at small s-d separations and/or low to moderate transport albedo $[a'=\mu_s'/(\mu_a+\mu_s')]$ have not undergone sufficient scattering to reach the diffusive regime,[6] there is the opportunity to use these signals to recover characteristics of the single-scattering phase function of the turbid medium.[7–10] Efforts have been undertaken by several groups to develop models for tissue reflectance that implement higher-order P_N and δ-P_N approximations in both infinite and semi-infinite geometries.[11–22] The effort most relevant to the prediction of spatially resolved diffuse reflectance from a semi-infinite turbid medium is that of Hull and Foster who developed the P_3 approximation for this case.[17] Their implementation provides for the accurate recovery μ_a and μ_s' from spatially resolved reflectance measurements made at small s-d separations for $(\mu_s'/\mu_a) \geq 1.43$.[17,19] However, assumptions taken with respect to both first- and second-order similarity relations prevent their implementation to recover characteristics of the single-scattering phase function.

Also of interest is the development of so-called δ-P_N (δ-Eddington) approximations.[11,12,15,16,18,20,23] These approximations add a Dirac-δ function to the Nth order Legendre polynomial expansion used to approximate the radiance and single-scattering phase functions. This improves the ability to model collimated sources and highly forward scattering media such as biological tissues. In biomedical optics, δ-P_N approximations were first investigated independently by Prahl[11] and by Star[12] with a primary interest in providing for improved predictions of optical dosimetry. More recently several groups have investigated the use of δ-P_1 and δ-P_3 approximations to predict the diffuse reflectance of homogeneous and layered systems when irradiated with a planar (one-dimensional) optical source.[16,18,20] Collectively, these studies have demonstrated that δ-P_N approximations provide substantial improvements in accuracy when compared to their P_N approximation counterpart. This fact, however, has not yet been exploited for prediction of spatially resolved diffuse reflectance from semi-infinite turbid media.

Our interest here is the development and analysis of the δ-P_1 approximation to provide improved estimates for spatially resolved reflectance from semi-infinite turbid media, especially at small s-d separations and for media with moderate or low albedo. While other analytical methods[17,24] (e.g., P_3 approximation, telegrapher's equations) have been examined specifically for this purpose, their use for the recovery of optical properties either remain untested (telegrapher's equation) or has been implemented in a fashion that removes the capacity to predict characteristics of the single scattering phase function. Computational approaches[25,26] [e.g., scaled or "white" Monte Carlo (MC) methods] have also been developed to recover successfully optical properties from spatially resolved reflectance measurements. However, a set of Monte Carlo simulations covering the relevant range of optical properties must be run and stored in advance. Moreover, different simulation sets must be run for different single-scattering phase functions of interest.

The objectives of this paper are twofold. First, we formulate a solution within the δ-P_1 approximation to predict the spatially resolved diffuse reflectance (SRDR) with “pencil” beam irradiation and compare the solution to predictions given by MC simulations and the SDA. Second, we evaluate the performance of the δ-P_1 solution to extract the optical absorption (μ_a), reduced scattering (μ_s'), and single-scattering asymmetry (g_1) coefficients from experimental measurements of SRDR in tissue phantoms. The analytical formulation permits a framework in which the radiative transport estimates can be computed rapidly, and configured easily to accommodate any single-scattering phase function of interest.

II. THEORY AND MODELING

II.A. Governing equations

We begin with the RTE that governs the spatial/angular distribution of the photon radiance $L(\mathbf{r}, \hat{\omega})$ within turbid media

$$\hat{\omega} \cdot \nabla L(\mathbf{r},\hat{\omega})=-\mu_t L(\mathbf{r},\hat{\omega})+\mu_s\int_{4\pi} L(\mathbf{r},\hat{\omega}')p(\hat{\omega}' \rightarrow \hat{\omega})d\hat{\omega}'+S(\mathbf{r},\hat{\omega}), \quad (1)$$

where

$\hat{\omega}'$, $\hat{\omega}$ = unit vectors representing the direction of light propagation before and after scattering, respectively,

$L(\mathbf{r}, \hat{\omega})$ = rate of photon arrival at position $\mathbf{r}$ in direction $\hat{\omega}$ [W m^{-2} sr^{-1}],

$S(\mathbf{r}, \hat{\omega})$ = volumetric source [W m^{-3} sr^{-1}],

$p(\hat{\omega}' \rightarrow \hat{\omega})$ = single-scattering phase function,

μ_t = total attenuation coefficient (=$\mu_a + \mu_s$) [m^{-1}],

μ_a = absorption coefficient [m^{-1}], and

μ_s = scattering coefficient [m^{-1}].

The derivation of the δ-P_1 approximation is identical to that of the SDA except that a Dirac-δ function is added to both the radiance and phase function approximations in order to decompose the light field into ballistic (unscattered) and diffuse components. The approximate form of the single-scattering phase function used in the δ-P_1 approximation is

$$p_{\delta-P_1}(\hat{\omega}' \rightarrow \hat{\omega})=\frac{1}{4\pi}[2f\delta(1-\hat{\omega}\cdot\hat{\omega}_0)+(1-f)p_{SDA}(\hat{\omega}' \rightarrow \hat{\omega})], \quad (2)$$

where $\hat{\omega}_0$ is the propagation direction of the collimated light, f is the fraction of the collimated light that is scattered directly forward, and p_{SDA} represents the phase function employed in the SDA

$$p_{SDA}(\hat{\omega}' \rightarrow \hat{\omega})=[1+3g^*(\hat{\omega}\cdot\hat{\omega}')], \quad (3)$$

where g^* is a single-scattering asymmetry coefficient used within the δ-P_1 formulation. Without the collimated term (f = 0), Eq. (2) returns to the phase function used in the SDA. The δ-P_1 phase function has two parameters f and g^* that are chosen to match the first and second moments of the actual single-scattering phase function of the medium to be modeled. In this study, we choose these parameters to best match the Henyey–Greenstein (H–G) phase function, because it has been shown experimentally to be a reasonable approximation to biological tissues.[27] Alternatively, other phase functions such as Rayleigh–Gans and Mie scattering that have been investigated to model successfully light transport in biological tissues can be employed easily within the δ-P_1 approximation.[28–30] Equating the first and second moments of the δ-P_1 phase function to the H–G phase function provides the following expressions for f and g^*:[23]

$$f = g_2 = g_1^2 \quad \text{and} \quad g^* = \frac{g_1 - g_2}{1 - g_2} = \frac{g_1}{1 + g_1}. \quad (4)$$

Substitution of Eqs. (2) and (3) into Eq. (1) results in a RTE with transformed parameters[10]

$$\widehat{\omega} \cdot \nabla L(\mathbf{r}, \widehat{\omega}) = -\mu_t^* L(\mathbf{r}, \widehat{\omega}) + \mu_s^* \int_{4\pi} L(\mathbf{r}, \widehat{\omega}') p^*(\widehat{\omega}, \widehat{\omega}') \mathrm{d}\widehat{\omega}' + S(\mathbf{r}, \widehat{\omega}), \quad (5)$$

where $\mu_s^* = \mu_s(1-f)$ and $\mu_t^* = \mu_a + \mu_s^*$. Note that this modified RTE is parameterized by (μ_a, μ_s^*,g^*) and not by (μ_a, μ_s, g_1). However, the addition of Dirac-δ functions to both phase function and radiance approximations introduces an additional degree of freedom that allows use of a second-order similarity relation. Following the approach of Bevilacqua and Depeursinge,[26] we define an additional optical parameter γ as

$$\gamma = \frac{1 - g_2}{1 - g_1} = 1 + g_1, \quad (6)$$

where the second equality shown is valid only when considering the H–G phase function. The combination of Eq. (6) with the relationships shown in Eq. (4) leads to the second-order similarity relation

$$\mu_s^* = \gamma \mu_s'. \quad (7)$$

Thus (μ_a, μ_s', γ) is chosen as the parameter set for resolution of the inverse problem described later in Sec. III.

In a manner similar to the phase function, the radiance approximation is also decomposed into diffuse [$L_d(\mathbf{r}, \hat{\omega})$] and ballistic [$L_b(\mathbf{r}, \hat{\omega})$] components:

$$L(\mathbf{r}, \widehat{\omega}) = L_d(\mathbf{r}, \widehat{\omega}) + L_b(\mathbf{r}, \widehat{\omega}). \quad (8)$$

The diffuse radiance is approximated as

$$L_d(\mathbf{r}, \widehat{\omega}) = \frac{1}{4\pi} \phi_d(\mathbf{r}) + \frac{3}{4\pi} j(\mathbf{r}) \cdot \widehat{\omega}, \quad (9)$$

where $\phi_d(\mathbf{r})$ is the diffuse fluence rate and $j(\mathbf{r})$ is the radiant flux. The ballistic (unscattered) radiance is given as

$$L_{\mathrm{b}}(\mathbf{r},\widehat{\omega})=\frac{1}{2\pi}E(\mathbf{r})\,\delta(1-\widehat{\omega}\cdot\widehat{\omega}_{\mathbf{0}}),\quad (10)$$

where $E(\mathbf{r})$ is the irradiance distribution of the light source. This decomposition of the radiance into ballistic and diffuse components enables the δ-P$_1$ approximation to provide estimates that are in agreement with the SDA when $(\mu_s'/\mu_a)\to\infty$ and the Beer–Lambert Law when $(\mu_s'/\mu_a)\to 0$.[15,20]

Substitution of Eqs. (8)–(10) into the modified RTE [Eq. (5)] provides the governing equations in the δ-P$_1$ approximation for semi-infinite turbid media:[31]

$$\nabla^2\phi_{\mathrm{d}}(\mathbf{r})-\mu_{\mathrm{eff}}^2\phi_{\mathrm{d}}(\mathbf{r})=-\frac{\mu_s^* E(\mathbf{r},\widehat{\mathbf{z}})}{D}\quad (11)$$

and

$$j(\mathbf{r})=-D[\nabla\phi_{\mathrm{d}}(\mathbf{r})-3g^*\mu_s^* E(\mathbf{r},\widehat{\mathbf{z}})\widehat{\mathbf{z}}],\quad (12)$$

where $\mu_{\mathrm{eff}} = (3\mu_a\mu_{\mathrm{tr}})^{1/2} = (\mu_a/D)^{1/2}$, $D = 1/3\mu_{\mathrm{tr}}$, $\mu_{\mathrm{tr}}=(\mu_a+\mu_s')$, and $\hat{\mathbf{z}}$ is the unit normal vector directed inward from the boundary. The collimated source is assumed to be directed perpendicularly to the surface as shown in Fig. 1 and expressed by the source function

$$E(\mathbf{r},\widehat{\mathbf{z}})=P_0(1-R_s)\exp(-\mu_t^* z),\quad (13)$$

where P_0 is the power of the source, and R_s is specular reflectance due to refractive index mismatch. This functional form represents a pencil beam located at $\rho = 0$ that is attenuated exponentially at the rate μ_t^* along the z axis as required of collimated sources within the δ-P$_1$ approximation.

II.B. Boundary conditions

To solve the governing equations, two boundary conditions are required. We adopt the approach of Haskell and co-workers and implement an extrapolated boundary condition that satisfies a zero fluence rate condition at an extrapolated boundary located at distance z_b outside the medium i.e., $\phi_d(\rho, z = -z_b) = 0$.[32] The value of z_b is calculated as

$$z_b=\left(\frac{1+R_1}{1-R_1}\right)\frac{2}{3\mu_{\mathrm{tr}}}=2AD,\quad (14)$$

where $A = (1 + R_1)/(1 - R_1)$ and R_1 is the first moment of the Fresnel reflection coefficient for unpolarized light. Figure 2 depicts the configuration of the source and image for a point source embedded at an arbitrary location z' within the semi-infinite body. The image source is placed in the air at a distance z' from the surface of the image medium which islocated at $z = -2z_b$. The second boundary condition requires the diffuse light field to vanish for regions far away from the source, i.e.,

$$\phi_{\mathrm{d}}(\mathbf{r})|_{\mathbf{r}\to\infty}\to 0.\quad (15)$$

II.C. Solution for pencil beam irradiation

The Green's function of the Helmholtz equation Eq. (11), at a point (ρ, z) due to a point source located at (0, z') in an unbounded medium in cylindrical coordinates is

$$G(\rho, z)=\frac{1}{4\pi D}\frac{\exp(-\mu_{\text{eff}}\rho_1)}{\rho_1}, \quad (16)$$

where $\rho_1 = [\rho^2 + (z - z')^2]^{1/2}$. To formulate the solution for a cylindrically axisymmetric semi-infinite medium using this Green's function that also satisfies the extrapolated boundary condition, we place a point source at (0, z') and an image point source at (0, $-2z_b - z'$). This results in the following Green's function for a point source in a semi-infinite medium:

$$G(\rho, z)=\frac{1}{4\pi D}\frac{\exp(-\mu_{\text{eff}}\rho_1)}{\rho_1}-\frac{1}{4\pi D}\frac{\exp(-\mu_{\text{eff}}\rho_2)}{\rho_2}, \quad (17)$$

where $\rho_2 = [\rho^2 + (z + z' + 2z_b)^2]^{1/2}$.

To get the desired solution in the δ-P$_1$ approximation we must perform a linear superposition of the distributed source term [Eq. (13)] and the semi-infinite Green's function [Eq. (17)]. This provides the following solution for the diffuse fluence rate within the δ-P$_1$ approximation for a semi-infinite turbid medium:

$$\phi_{\text{d}}(\rho, z)=\frac{a^*}{4\pi D}\int_0^\infty\left[\frac{\exp(-\mu_{\text{eff}}r_1)}{r_1}-\frac{\exp(-\mu_{\text{eff}}r_2)}{r_2}\right]\times\exp(-\mu_t^* z')\text{d}z', \quad (18)$$

where $a^*=\mu_s^*/\mu_t^*$. Numerical estimation of the semi-infinite integration in Eq. (18) is executed via Gaussian quadrature employing a Laguerre polynomial weighting function (MAT-LAB, Mathworks Inc., Natick, MA).

II.D. Spatially resolved diffuse reflectance (SRDR)

The fluence rate expression [Eq. (18)] is obtained by the application of an extrapolated boundary condition. This extrapolated boundary condition is an approximation to the Marshak (or partial-current) boundary condition that conserves the diffuse radiance at the tissue-air interface. This is expressed by[33]

$$\int_{\widehat{\omega}\cdot\widehat{\mathbf{z}}>0}L_{\text{d}}(\mathbf{r},\widehat{\omega})(\widehat{\omega}\cdot\widehat{\mathbf{z}})\text{d}\widehat{\omega}=\int_{\widehat{\omega}\cdot\widehat{\mathbf{z}}<0}L_{\text{d}}(\mathbf{r},\widehat{\omega})r_{\text{F}}(-\widehat{\omega}\cdot\widehat{\mathbf{z}})(-\widehat{\omega}\cdot\widehat{\mathbf{z}})\text{d}\widehat{\omega}, \quad (19)$$

where $r_F(-\hat{\boldsymbol{\omega}}\cdot\hat{\mathbf{z}})$ is the Fresnel reflection coefficient for un-polarized light. This equation equates the amount of diffuse light that travels upward ($\hat{\boldsymbol{\omega}}\cdot\hat{\mathbf{z}} < 0$) and gets internally reflected at the interface with the amount of diffuse light traveling downward ($\hat{\boldsymbol{\omega}}\cdot\hat{\mathbf{z}} \geq 0$) from the interface. Substitution of the diffuse radiance approximation and removal of the radiant flux [$j(\mathbf{r})$] term using Eq. (12) gives

$$[\phi_{\text{d}}(\mathbf{r})-2AD\nabla\phi_{\text{d}}(\mathbf{r})\cdot\widehat{\mathbf{z}}]|_{z=0}=-6ADg^*\mu_s^*E(\mathbf{r},\widehat{\mathbf{z}})|_{z=0}. \quad (20)$$

This leads to the following expression for the diffuse reflectance within δ-P$_1$ approximation:[20]

$$R_d = -D\nabla\phi_d(\rho, z)\cdot(-\hat{\mathbf{z}})|_{z=0} = \frac{\phi_d(z=0)}{2A}. \quad (21)$$

II.E. Monte Carlo simulations

To assess the quality of the predictions provided by the δ-P$_1$ approximation, we compare these results to predictions provided by Monte Carlo (MC) simulations. The MC simulation was written "in-house" and provides an exact solution to the RTE within statistical uncertainty. The code uses discrete absorption weighting and a terminal estimator within a cylindrical axisymmetric semi-infinite geometry. We performed MC simulations for pencil beam illumination to provide the SRDR over the range $\rho \in [0, 15]$ mm at 0.1 mm intervals. The number of photons launched for each run is dependent on the optical properties of the media and chosen in the range of 10^7–10^{10} to achieve a relative standard deviation in the predicted reflectance of <0.1% at all s-d separations. The H–G phase function was used as the single-scattering phase function and photons that arrive at the tissue surface obey the Fresnel relations. All exiting photons contribute to the tally for the reflectance at the appropriate s-d separation ρ.

II.F. Standard diffusion approximation

We also assess the quality of the δ-P$_1$ approximation predictions relative to the standard diffusion approximation (SDA). There are various options for the calculation of spatially resolved reflectance within the SDA. We adopt the approach developed by Kienle and Patterson[4,34] as it represents the culmination of the examination of this problem by several groups,[3,32,35–37] and has been shown to provide the most accurate expressions for the spatially resolved reflectance within the SDA.[4,34] Moreover, both the solutions developed by Kienle and Patterson as well as the proposed δ-P$_1$ model utilize extrapolated boundary conditions and examine the case of detection over the outward-directed hemisphere. Kienle and Patterson give the following expression for the SRDR derived using an extrapolated boundary condition for a turbid medium with refractive index $n = 1.4$:

$$R(\rho) = 0.118\phi_d(\rho, z=0) + 0.306\, j(\rho), \quad (22)$$

where ϕ_d is fluence rate and j is radiant flux across the boundary. The fluence and radiant flux terms within the SDA are calculated from

$$\phi_d(\rho, z) = \frac{1}{4\pi D}\left(\frac{\exp\{-\mu_{\text{eff}}[(z-l^*)^2+\rho^2]^{1/2}\}}{[(z-l^*)^2+\rho^2]^{1/2}} - \frac{\exp\{-\mu_{\text{eff}}[(z+l^*+2z_b)^2+\rho^2]^{1/2}\}}{[(z+l^*+2z_b)^2+\rho^2]^{1/2}}\right), \quad (23)$$

$$j(\rho) = \frac{1}{4\pi}\left[l^*\left(\mu_{\text{eff}}+\frac{1}{r_1}\right)\frac{\exp(-\mu_{\text{eff}} r_1)}{r_1^2} + (l^*+2z_b)\left(\mu_{\text{eff}}+\frac{1}{r_2}\right)\frac{\exp(-\mu_{\text{eff}} r_2)}{r_2^2}\right], \quad (24)$$

where $r_1^2 = l^{*2} + \rho^2$ and $r_2^2 = (l^*+2z_b)^2 + \rho^2$.

III. ALGORITHM DEVELOPMENT FOR RECOVERY OF OPTICAL PROPERTIES

Following an approach similar to that proposed by Hayakawa and co-workers,[10] we designed and tested a three-stage optimization algorithm to extract optical properties over a broad range of (μ_s'/μ_a) from SRDR measurements. In this algorithm we first estimate l^* of the turbid medium from the SRDR measurement and use this to identify s-d positions that are sensitive to the specific optical properties we wish to recover. For instance, the photons collected at (ρ/l^*) ≫ 1 have experienced multiple scattering events and, for a highly scattering medium, the slope of the SRDR on a semilog plot is characterized by the effective attenuation coefficient, $\mu_{\mathrm{eff}} = [3\mu_a\mu_{\mathrm{tr}}]^{1/2}$. Thus SRDR data in this range of s-d separation contain information related to μ_a and μ_s'. By contrast, the SRDR data at (ρ/l^*) ≲ 2 are sensitive to g_1 and g_2. These factors influenced the design and testing of a three-stage algorithm depicted in Fig. 3.

Each stage of the algorithm is performed by executing a constrained Levenberg–Marquardt (LM) algorithm (MAT-LAB, Mathworks Inc., Natick, MA) that seeks to minimize a sum of squares, χ^2, between the measurements and the predictions of the SRDR given by the δ-P$_1$ approximation. Expressed mathematically this algorithm attempts to minimize

$$\chi^2(\mu_a, \mu_s', \gamma) = \sum_{i=1}^{M} \left[\frac{I_m(r_i) - I_p(r_i; \mu_a, \mu_s', \gamma)}{\sigma_i} \right]^2, \quad (25)$$

where $I_m(r_i)$ is the diffuse reflectance measured at location $\rho = r_i$, σ_i is the standard deviation of the measurement at $\rho = r_i$, I_p is the reflectance as predicted by Eq. (21) with optimizing parameters μ_a, μ_s', and γ, and M is the number of source-detector locations in the measurement set. Estimates for g_1 are then obtained from Eq. (6). To ensure full sampling of the parameter space and avoid convergence to a local minimum, ten trials of the LM algorithm are executed at each stage using initial guesses of the optical properties selected randomly from ranges relevant to biological tissues: $\mu_a \in [10^{-4}, 10^{-1}]$ mm^{-1}, $\mu_s' \in [0.03, 3]$ mm^{-1}, and $g_1 \in [0.6, 0.99]$. The range of g_1 is chosen because most biological tissues are highly forward scattering. In stage 3, we expand the range of random sampling to $g_1 \in [0.0, 0.99]$. Of the converged parameters for ten trials, the recovered parameter set that provides the lowest χ^2 value is selected as a best fit.

In stage 1 of the algorithm, the entire range of measured data is used to provide an initial estimate of the transport mean free path l^*. Although estimates for all three parameters are obtained from minimizing χ^2, only the l^* calculation is utilized to identify the range of s-d separations to be processed in the second stage of the algorithm.

In stage 2, we consider only SRDR measurements acquired at s-d separations $\rho > 0.5l^*$ to determine μ_a and μ_s'. The removal of SRDR data at $\rho < 0.5l^*$ is due to the fact that the SRDR estimates provided by the δ-P$_1$ approximation do not display the proper sensitivity to g_1 in this region. This will be demonstrated in the Results section (V, Fig. 6). Of the recovered values, μ_a, μ_s', and γ, only μ_a, μ_s', and the newly calculated l^* are saved as final optical parameters. The new estimate of l^* is then used in the final stage of the algorithm to identify the range of data most useful for the recovery of g_1.

Stage 3 is a single parameter optimization step. We fix the two parameters μ_a and μ_s' at the values obtained in stage 2, and run the LM algorithm to find γ. The range of SRDR measurements supplied to the optimization algorithm is $\rho > 1.5l^*$. This range is selected since the simulation results in Fig. 6 demonstrated that the δ-P$_1$ approximation provides accurate radiative transport estimates in this region and display the proper sensitivity to g_1. Since γ is a combination g_1 and g_2, we obtain g_1 from Eq. (6) with the implicit assumption that the medium is well characterized by the H–G phase function.

IV. EXPERIMENT MATERIALS AND METHODS

IV.A. Tissue phantom preparation

To test the proposed model and the inversion algorithm above, we developed two optical phantoms systems based on deionized water and polydimethylsiloxane (PDMS). The water-based optical phantoms utilize Intralipid (B. Brown, Irvine, CA) for optical scattering and Nigrosin (Sigma-Aldrich, St. Louis, MO) for optical absorption. The reduced scattering coefficient (μ_s') and asymmetry coefficient (g_1) were estimated using results from van Staveren and co-workers.[38] The absorption properties of the Nigrosin were determined using standard spectrophotometer measurements of multiple samples of Nigrosin dissolved in deionized water at various concentrations. Thus the preparation of a liquid phantom involved combining measured amounts of Intralipid and Nigrosin stock solutions with an appropriate volume of deionized water to attain the desired absorption and scattering properties. The phantoms were prepared to fill a cylindrical container (80 mm diameter × 100 mm height) in which they were measured.

PDMS was chosen as the base material for the solid phantoms as it possesses optical transparency, a refractive index similar to biological tissue ($n = 1.4$), and no endogenous fluorescence in the spectral range of interest. To introduce optical scattering and absorption in the PDMS, we used aluminum oxide (Al_2O_3, Sigma-Aldrich) and alcohol soluble Nigrosin, respectively. Aluminum oxide is used widely as a source of optical scattering due to its stability in PDMS and well-defined particle size distribution.[39] Additionally, we chose aluminum oxide because it provides the opportunity to fabricate a tissue-like phantom with an asymmetry coefficient (g_1) similar to biological tissues (~0.9) and markedly higher than that of Intralipid (~0.7). The Al_2O_3 particles were sent to Beckman Coulter Inc. for particle size analysis. From the particle size distribution, we determined the scattering coefficient and asymmetry parameter using Mie theory and the known refractive indices of the PDMS and Al_2O_3 particles. Precalculated amounts of PDMS, methanol-dissolved Nigrosin, and Al_2O_3 were thoroughly combined using a planetary mixer (AR-250, Thinky Corp., Japan) and poured into a mold for a curing process with the addition of a curing agent. The phantom after the curing process was cylindrical in shape with a 75 mm diameter and 40 mm height.

Tables I and II provide the optical properties of the four liquid and four solid phantoms at the wavelength used for the measurements, λ= 632.8 nm. These tables also specify the range of s-d separations provided to the inversion algorithm for recovery of optical properties.

IV.B. Spatially resolved diffuse reflectance measurements

A general schematic of the measurement setup is shown in Fig. 4. The SRDR measurements were obtained by a charge coupled device (CCD) camera mounted with its optical axis normal to the phantom surface. A He–Ne laser emitting at λ= 632.8 nm was coupled to a 200-μm-diam multimode optical fiber through a collimating lens. A neutral density filter is placed between the laser and the fiber to attenuate the intensity of the light source delivered to the sample. To ensure that specular reflection was not captured, a rectangular-shaped fiber optic illuminator (30 mm long ×4 mm wide×5 mm high) was designed and fabricated (Fiberguide, Stirling, NJ) to deliver light to the sample and block specular reflection from reaching the camera. The illuminator was composed of a right-angle microprism 0.5 mm in size coupled to an optical fiber with 0.12 numerical aperture. The prism was used for deflecting light from the fiber for perpendicular illumination of the medium. The use of this illuminator enabled the acquisition of quality images at locations proximal to laser source without saturation of the CCD and enabled the utilization of the full dynamic range of the camera. This is especially important to verify the accuracy of δ-P_1 approximation, because measurements at s-d separations comparable to a l^* display significant sensitivity to the moments of single-scattering phase function. A more detailed description of the illuminator performance can be found in our previous work using this system.[40]

The reflectance images were obtained by placing the phantom surface 18 cm below a 35 mm photographic lens at f/2.8 (Nikon, Japan) coupled to a thermoelectrically cooled 16 bit CCD camera (Photometrics, Tucson, AZ). A square area of the phantom surface 3.7 cm×3.7 cm in dimension was imaged onto the CCD chip with spatial resolution of ≈70 μm. Fifteen images were acquired for each sample and the average and standard deviation of the pixel intensity as a function of radial position away from the source was acquired to obtain the SRDR measurements.

The raw measurements represent a convolution of the true image and the instrument response of the optical signal. Thus to extract the true SRDR data we must remove the effect of the instrument response from the raw images. To convert the measured intensity to an absolute SRDR measurement, we performed a calibration procedure described by Pham and co-workers[41] which was also utilized in our previous study.[40] This procedure consists of two steps. First, images of the diffuse reflectance are acquired from a reference phantom with known optical properties. These "calibration images" were taken using the same settings as those used for measurements of the tissue phantoms. The instrument response of the system is then calculated using the data obtained from the reference phantom and a prediction of the diffuse reflectance generated by a MC simulation using the optical properties of the reference phantom. Specifically, the raw image measured by the CCD (I_R) is a convolution of the true image (I_T) and the instrument response (I_{IR}), which can be described as

$$I_R = I_T \otimes I_{IR}. \quad (26)$$

When Eq. (26) is Fourier transformed into the spatial frequency domain, the convolution operation is reduced to a simple multiplication, so that the instrument response can be determined by the division of the Fourier transform of the raw image intensity by the Fourier transform of the "true" image intensity as provided by the MC simulation. Using this instrument response, any measured intensity data can be converted into absolute reflectance (R_{abs}) using the following relationship:

$$R_{abs} = \mathscr{F}^{-1}\left[\frac{\mathscr{F}(I_R)}{\mathscr{F}(I_{IR})}\right], \quad (27)$$

where $\mathscr{F}$ and $\mathscr{F}^{-1}$ represent the Fourier and inverse Fourier transform, respectively. The converted intensity data are then supplied to the δ-P_1 inversion algorithm for extraction of optical properties.

V. RESULTS AND DISCUSSION

V.A. Forward problem results: SRDR predictions

Figure 5 displays the SRDR predictions provided by the δ-P_1 approximation, the SDA, and the MC simulations. A subplot is also shown that provides the percentage error between both the δ-P_1 and standard diffusion approximations relative to the MC simulation results. The optical properties considered are μ_a = 0.01/mm, g_1 = 0.9, and n = 1.4, with (μ_s'/μ_a)=100 and 10 for plots 3(a) and 3(b), respectively. The spatial scale for the source-detector separation ρ is normalized relative to the transport mean free path l^*.

There are several notable features in these results. First, all methods provide largely comparable SRDR predictions for (ρ/l^*)>3. However, the predictions provided by the SDA provide a slight ($\gtrsim$ 5%) but distinct offset from the MC results in the region where the SDA is expected to be accurate ($\rho \gg l^*$). In this same region, the δ-P$_1$ approximation provides accurate predictions with vanishing relative error for both $(\mu_s'/\mu_a)=100$ and 10.

Second, for $(\mu_s'/\mu_a)=10$, the relative error in the predictions provided by both δ-P$_1$ and SDA models is a bit larger than those provided for $(\mu_s'/\mu_a)=100$. For $(\mu_s'/\mu_a)=100$ the relative error provided by both δ-P$_1$ and standard diffusion approximations is <10% for (ρ/l^*)>1. However, for $(\mu_s'/\mu_a)=10$ the relative error provided by the δ-P$_1$ approximation is consistently <10% only for (ρ/l^*)>2. For the SDA, this level of accuracy is consistently present only for (ρ/l^*)>3.

Third, the standard diffusion and δ-P$_1$ approximations underestimate the reflectance considerably for (ρ/l^*) $\lesssim$ 0.5 and (ρ/l^*)$\lesssim$0.2, respectively. The reflectance estimates provided by the δ-P$_1$ approximation are slightly better over all for detector locations as small as (ρ/l^*)= 0.1 and, importantly, provide an SRDR profile with the proper curvature. Finally, both the δ-P$_1$ and standard diffusion approximations overestimate significantly the reflectance in a small region of (ρ/l^*) ≈ 0.5–1.5. Within this region there is usually a small interval of s-d separations where the SDA outperforms the δ-P$_1$ model.

Figure 6 displays predictions for the SRDR provided by the standard diffusion and δ-P$_1$ approximations as compared to a MC simulation for a fixed $(\mu_s'/\mu_a)=30$ for two different values of g_1 = 0.9 and 0.5. To highlight the differences, the SRDR is plotted on a linear scale and the relative error of the SDA and δ-P$_1$ models as compared to the MC results is shown in the bottom panel. The results show clearly that the SRDR is affected by the value of g_1 for (ρ/l^*)$\lesssim$2. Interestingly for (ρ/l^*)>0.8, both the δ-P$_1$ and MC results show that a reduction in g_1 from 0.9 to 0.5 results in a decrease in the reflectance. For both g_1 = 0.9 and 0.5, the δ-P$_1$ model provides more accurate reflectance estimates than the SDA for all s-d separations except (ρ/l^*) ≈ 0.4–0.8. Moreover, as expected, the SRDR estimates provided by the SDA display no sensitivity to g_1.

Another important feature in this figure is that MC results for g_1 = 0.5 and g_1 = 0.9 cross at (ρ/l^*)≃0.8. This is because as the asymmetry coefficient g_1 increases, the light distribution becomes more forward directed near the source, and the intensity of backscattered light decreases. However, the predictions provided by the δ-P$_1$ model show no such crossing of the SRDR for these g_1 values. This is the principal reason for why data collected at ρ<0.5l^* are excluded from the inversion algorithm for optical property determination.

These results are consistent with the findings of Bevilacqua and Depeursinge who demonstrated that the influence of g_1 and g_2 on the SRDR for highly scattering media is significant for (ρ/l^*) ≈ 1 and 0.5< (ρ/l^*)<2, respectively, while the effect of higher-order moment g_n influences are important at shorter s-d separations [(ρ/l^*)$\lesssim$0.3].[26] The impact of the characteristics of the single-scattering phase function on the SRDR proximal to the laser source as well as their impact on the determination of optical properties using the SDA have been considered by other investigators.[26,29,42]

V.B. Inverse problem results: Optical property recovery

V.B.1. Liquid optical phantoms—For measurements taken from the liquid phantoms, the estimated values for μ_a, μ_s', and l^* and their associated relative error after the first stage of the δ-P$_1$ approximation based inversion algorithm are presented in Table III. The optical property range of the tested phantoms span $(\mu_s'/\mu_a)=117$ to 6. These results are what would have been attained using a single-stage inversion procedure using the entire measured data set. The estimation errors are ±25%, ±23%, and ±21% for μ_a, μ_s', and l^*, respectively. The results from the phantom with the largest scattering $[(\mu_s'/\mu_a)=117]$ display the greatest μ_a error of 25%. This is likely due to the fact that the largest s-d separation used in the measurement set, ρ = 7 mm, collects photons that have not traveled sufficiently long path lengths within the sample necessary for the accurate determination of such a low value of μ_a. Apart from the $(\mu_s'/\mu_a)=117$ case, the results exhibit increasing estimation error with decreasing (μ_s'/μ_a). The relatively large error in the first stage indicates that simultaneous recovery of the optical parameters in a single stage inversion procedure using the entire measurements may not be the best strategy. The value of l^* is utilized to supply the appropriate subset of SRDR data to the subsequent stages of the algorithm.

The final recovered values and relative errors of μ_a, μ_s', l^*, and g_1 recovered by the multi-stage δ-P_1 algorithm are summarized in Table IV. Also included, for easy comparison, are the results given by stage 1 of the algorithm. The final values for μ_a, μ_s' and l^* are obtained from stage 2 of the algorithm while g_1 is obtained from stage 3. These results show that the multistage inversion procedure based on the δ-P_1 approximation recover μ_a, μ_s' and l^* with relative errors of no worse than ±22%, ±17%, and ±15%, respectively. These results exhibit errors that are typically 3%–5% lower than the results shown in stage 1 and illustrate the benefit of our multi-staged algorithm. The enhanced precision of l^* from stage 2 enabled recovery of g_1 within ±17% error. This modest accuracy in the recovery of g_1 is potentially significant as indicated by a recent study by Charvet and co-workers.[43] This study reported the changes in optical properties of *in vivo* mouse skin produced by the administration of topical agents that promote either inflammatory or carcinogenic response without any obvious change to visual appearance of the skin surface. These measurements revealed changes in the γ parameter over the wavelength range λ = 480–550 nm that are equivalent to a 30%–50% reduction in g_1.[43]

To assess the performance of this δ-P_1 approximation based inversion procedure, we also recovered optical properties using SRDR estimates provided by the SDA. For the SDA-based inversion, the entire range of data is supplied to the algorithm to recover μ_a, μ_s' and l^* in a single stage. The inclusion of reflectance data proximal to the source should not penalize or otherwise hamper the SDA inversion procedure. In fact an earlier study by Kienle-and co-workers demonstrated that the exclusion of data points close to the source results in a poorer recovery of μ_a and μ_s'.[44] The SDA-based inversion recovered μ_a, μ_s', and l^* with relative errors of ±29%, ±20%, and ±16%, respectively. The optical properties recovered using the SDA approach are typically worse in accuracy than the values recovered even after stage 1 of the δ-P_1 multi-stage algorithm. On a case by case basis, the final optical property values recovered by δ-P_1-based inversion procedure possess comparable or substantially improved accuracy as compared to the values recovered using the SDA approach. Moreover the δ-P_1-based approach does a reasonable job in recovering the single-scattering asymmetry coefficient g_1; a capability that an SDA-based inversion lacks.

Figure 7 displays the measured SRDR data for the four tested phantoms along with the δ-P_1 and standard diffusion approximation predictions at the recovered set of optical properties. The δ-P_1 predictions better model the curvature of the SRDR measurements proximal to the source and also provide a better fit to the SRDR data at large s-d separations.

V.B.2. Solid optical phantoms—We have applied the multi-staged algorithm described in Sec. III to determine μ_a, μ_s' and g_1 from SRDR measurements of the Al_2O_3 siloxane phantoms that possess a significantly larger single-scattering asymmetry coefficient (g_1 = 0.88) than the Intralipid phantoms (g_1 = 0.74). Table V provides the recovered values after stage 1 while Table VI provides both the stage 1 and final results from the δ-P_1 inversion algorithm as well as the recovered values using the SDA approach. These predictions result from experimental SRDR measurements on a series of PDMS based phantoms whose optical property values span $(\mu_s'/\mu_a)=81$ to 4 and are shown in Table II. As in the Intralipid phantoms, we see that the final results exhibit relative errors 3%–5% lower than the results obtained in stage 1 and emphasize the benefit of our multi-staged algorithm. Overall, the δ-P_1 approximation based inversion algorithm provided optical property estimates with relative error no worse than ±17%, ±18%, and ±21% for μ_a, μ_s', and l^*, respectively. By comparison, optical property recovery using the SDA-based inversion resulted in relative errors of ±28%, ±25%, and ±28% for μ_a, μ_s', and l^*, respectively, and are typically worse than the results obtained even by stage 1 of the δ-P_1 inversion approach. Unlike the results for the Intralipid phantoms, the recovered optical properties in the sample with the highest scattering $(\mu_s'/\mu_a)=80$ exhibit very small errors even for μ_a. This is due to the smaller transport mean free path of the solid phantoms that allowed the photons collected at the large s-d separations to travel sufficiently large path lengths in the sample and provide sensitivity to the low value of μ_a. Similar to the Intralipid-based phantoms, the capacity to extract optical properties using both the δ-P_1 and standard diffusion approximation based procedures generally degrades as (μ_s'/μ_a) decreases. Nevertheless, the δ-P_1 almost invariably outperforms the SDA and, in addition, recovers g_1 with an error no worse than ±17%.

Figure 8 displays the measured data for the four tested phantoms along with the δ-P_1 and SDA model predictions at the recovered set of optical properties. Again, we see that the δ-P_1 approximation generally provides better reflectance predictions, both with the curvature of the SRDR proximal to the source as well as better congruence with the SRDR data at large s-d separations.

VI. SUMMARY AND CONCLUSIONS

We have presented governing equations and solution for the spatially resolved diffuse reflectance from a semi-infinite turbid media within the δ-P_1 approximation to the radiative transport equation. We have shown that the radiative transport predictions provided by the δ-P_1 model are generally more accurate than those provided by the standard diffusion approximation through comparison with the results of Monte Carlo simulations. This superior performance is achieved by the addition of a Dirac-δ function to both the radiance and single-scattering phase function approximations. This consideration results in better estimation of the spatially resolved reflectance close to light source and for media of low albedo.

The addition of the Dirac-δ function to both the radiance and single-scattering phase function approximations provides an extra degree of freedom that allows the radiative transport predictions to be sensitive to the single-scattering asymmetry coefficient g_1. We have demonstrated that the δ-P_1 approximation provides radiative transport estimates that model accurately the effect of g_1 on the spatially resolved diffuse reflectance for $(\rho/l^*) \gtrsim 0.8$.

The excellent performance of the δ-P$_1$ approximation prompted us to develop a multi-stage inversion algorithm to recover μ_a, μ_s', and g_1 from spatially resolved diffuse reflectance measurements. These measurements were made on liquid and polymer tissue phantoms that utilized Intralipid and Al_2O_3 particles, respectively, for scattering, and Nigrosin for optical absorption with a wide range of (μ_s'/μ_a) and varying g_1.

For the extraction of optical properties, the δ-P$_1$ model within a multi-staged inversion algorithm is validated both for liquid and solid phantoms. This algorithm has demonstrated the recovery of μ_a, μ_s' and l^* within ±22%, ±18% and ±21% in liquid and solid phantoms with $4<(\mu_s'/\mu_a)<117$. Moreover, the ability of the δ-P$_1$ approximation to provide radiative transport estimates with sensitivity to g_1 enable the recovery of g_1 to within ±17%. By comparison, the SDA-based inversion procedure demonstrated the recovery of μ_a, μ_s' and l^* with errors of ±29%, ±25%, and ±28%, respectively. Our SDA results are comparable to those obtained by studies that employ the SDA for optical property recovery.[4]

In conclusion, we have developed and validated an analytic solution within the δ-P$_1$ approximation along with a multi-stage inversion algorithm for optical property determination for homogeneous turbid media using SRDR measurements acquired from a CCD camera platform. Our δ-P$_1$ approximation based approach determines optical properties from spatially resolved reflectance measurements over a wide range of tissue optical properties with accuracy that surpasses the capabilities of standard diffusion approximation based approaches. In particular, the recovery of g_1 from measurements made at s-d separations comparable to l^* is an indication of the usefulness of the δ-P$_1$ approach.

Acknowledgments

We are grateful to the National Institutes of Health for support under Grant Nos. P41-RR-01192 (Laser Microbeam and Medical Program) and R01-EB-00345.

References

1. Kim AD. Transport theory for light propagation in biological tissue. J Opt Soc Am A. 2004; 21(4): 820–827.
2. Fantini S, Franceschini MA, Gratton E. Semi-infinite-geometry boundary problem for light migration in highly scattering media: A frequency-domain study in the diffusion approximation. J Opt Soc Am B. 1994; 11(10):2128–2138.
3. Hielscher AH, Jacques SL, Wang L, Tittel FK. The influence of boundary conditions on the accuracy of diffusion theory in time-resolved reflectance spectroscopy of biological tissues. Phys Med Biol. 1995; 40(11):1957–1975. [PubMed: 8587943]
4. Kienle A, Patterson MS. Determination of the optical properties of semi-infinite turbid media from frequency-domain reflectance close to the source. Phys Med Biol. 1997; 42(9):1801–1819. [PubMed: 9308085]
5. Vogel A, Venugopalan V. Mechanisms of pulsed laser ablation of biological tissues. Chem Rev (Washington, DC). 2003; 103(2):577–644.
6. You JS, Hayakawa CK, Venugopalan V. Frequency domain photon migration in the δ-P$_1$ approximation: Analysis of ballistic, transport and diffuse regimes. Phys Rev E. 2005; 72(2): 021903.
7. Jones MR, Yamada Y. Determination of the asymmetry parameter and scattering coefficient of turbid media from spatially resolved reflectance measurements. Opt Rev. 1998; 5(2):72–76.
8. Bevilacqua F, Piguet D, Marquet P, Gross JD, Jakubowski D, Venugopalan V, Tromberg BJ, Depeursinge C. Superficial tissue property determination using spatially resolved measurements close to the source: Comparison with frequency domain photon migration measurements. Proc SPIE. 1999; 3597:540–547.

9. Bevilacqua F, Depeursinge C. Monte Carlo study of diffuse reflectance at source-detector separations close to one transport mean free path. J Opt Soc Am A. 1999; 16(12):1935–1945.
10. Hayakawa CK, Hill BY, You JS, Bevilacqua F, Spanier J, Venugopalan V. Use of the delta-P_1 approximation for recovery of optical absorption, scattering, and asymmetry coefficients in turbid media. Appl Opt. 2004; 43(24):4577–4584.
11. Prahl, SA. PhD thesis. University of Texas; Austin: 1988. Light Transport in Tissue.
12. Star, WM. Dosimetry of Laser Radiation in Medicine and Biology. Müller, GJ.; Sliney, DH., editors. SPIE; Bellingham, WA: 1989. p. 146-154.
13. Boas DA, Liu H, O'Leary MA, Chance B, Yodh AG. Photon migration within the P_3 approximation. Proc SPIE. 1995; 2389:240–247.
14. Dickey D, Barajas O, Brown K, Tulip J, Moore RB. Radiance modelling using the P3 approximation. Phys Med Biol. 1998; 43(12):3559–3570. [PubMed: 9869032]
15. Venugopalan V, You JS, Tromberg BJ. Radiative transport in the diffusion approximation: An extension for highly absorbing media and small source-detector separations. Phys Rev E. 1998; 58(2):2395–2407.
16. Spott T, Svaasand LO. Collimated sources in the diffusion approximation. Appl Opt. 2000; 39(34): 6453–6465. [PubMed: 18354660]
17. Hull EL, Foster TH. Steady-state reflectance spectroscopy in the P_3 approximation. J Opt Soc Am A. 2001; 18(3):584–599.
18. Fawzi YS, Youssef ABM, El-Batanony MH, Kadah YM. Determination of the optical properties of a two-layer tissue model by detecting photons migrating at progressively increasing depths. Appl Opt. 2003; 42(31):6398–6411. [PubMed: 14649284]
19. Finlay JD, Foster TH. Hemoglobin oxygen saturations in phantoms and *in vivo* from measurements of steady-state diffuse reflectance at a single, short source-detector separation. Med Phys. 2004; 31(7):1949–1959. [PubMed: 15305445]
20. Carp SA, Prahl SA, Venugopalan V. Radiative transport in the delta-P_1 approximation: Accuracy of fluence rate and optical penetration depth predictions in turbid semi-infinite media. J Biomed Opt. 2004; 9(3):632–647. [PubMed: 15189103]
21. Xu H, Farrell TJ, Patterson MS. Investigation of light propagation models to determine the optical properties of tissue from interstitial frequency domain fluence measurements. J Biomed Opt. 2006; 11(4):041104. [PubMed: 16965132]
22. Chin LC-L, Whelan WM, Vitkin IA. Information content of point radiance measurements in turbid media: Implications for interstitial optical property quantification. Appl Opt. 2006; 45(9):2101–2114. [PubMed: 16579581]
23. Joseph JH, Wiscombe WJ, Weinman JA. The delta-Eddington approximation for radiative flux transfer. J Atmos Sci. 1976; 33:2452–2459.
24. Durian DJ, Rudnick J. Spatially resolved backscattering: Implementation of extrapolation boundary condition and exponential source. J Opt Soc Am A. 1999; 16(4):837–844.
25. Kienle A, Patterson MS. Determination of the optical properties of turbid media from a single Monte Carlo simulation. Phys Med Biol. 1996; 41(10):2221–2227. [PubMed: 8912392]
26. Bevilacqua F, Piguet D, Marquet P, Gross JD, Tromberg BJ, Depeursinge C. In vivo local determination of tissue optical properties: Applications to human brain. Appl Opt. 1999; 38(22): 4939–4950. [PubMed: 18323984]
27. Jacques SL, Alter CA, Prahl SA. Angular dependence of HeNe laser light scattering by human dermis. Lasers Life Sci. 1987; 1:309–333.
28. Graaff R, Aarnoudse JG, de Mul FFM, Jentink HW. Similarity relations for anisotropic scattering in absorbing media. Opt Eng (Bellingham). 1993; 32:244–252.
29. Kienle A, Forster FK, Hibst R. Influence of the phase function on determination of the optical properties of biological tissue by spatially resolved reflectance. Opt Lett. 2001; 26(20):1571–1573. [PubMed: 18049666]
30. Nilsson H, Larsson M, Nilsson GE, Strömberg T. Optical sectioning using a fiber probe with an angled illumination-collection geometry: Evaluation in engineered tissue phantoms. J Biomed Opt. 2002; 7(3):478–485. [PubMed: 12175300]

31. Star, WM. Diffusion theory of light transport. In: Welch, AJ.; van Gemert, MJC., editors. Optical-Thermal Response of Laser-Irradiated Tissue. Plenum; New York: 1995. p. 131-206.
32. Haskell RC, Svaasand LO, Tsay T-T, Feng T-C, McAdams MS, Tromberg BJ. Boundary conditions for the diffusion equation in radiative transfer. J Opt Soc Am A. 1994; 11(10):2727–2741.
33. Case, KM.; Zweifel, PF. Linear Transport Theory. Addison–Wesley; Reading, MA: 1967.
34. Kienle A, Patterson MS. Improved solutions of the steady-state and the time-resolved diffusion equations for reflectance from a semi-infinite turbid medium. J Opt Soc Am A. 1997; 14(1):246–254.
35. Groenhuis RAJ, Ferverda HA, Ten Bosch JJ. Scattering and absorption of turbid materials determined form reflection measurements 1: Theory. Appl Opt. 1983; 22(16):2456–2462. [PubMed: 18196156]
36. Groenhuis RAJ, Ten Bosch JJ, Ferverda HA. Scattering and absorption of turbid materials determined form reflection measurements 2: Measuring method and calibration. Appl Opt. 1983; 22(16):2463–2467. [PubMed: 18196157]
37. Farrell TJ, Patterson MS, Wilson B. A diffusion theory model of spatially resolved, steady-state diffuse reflectance for the noninvasive determination of tissue optical properties in vivo. Med Phys. 1992; 19(4):879–888. [PubMed: 1518476]
38. van Staveren HJ, Moes CJM, van Marle J, Prahl SA, van Gemert MJC. Light scattering in Intralipid-10% in the wavelength range of 400– 1100 nm. Appl Opt. 1991; 30(31):4507–4514. [PubMed: 20717241]
39. Pogue BW, Patterson MS. Review of tissue simulating phantoms for optical spectroscopy, imaging, and dosimetry. J Biomed Opt. 2006; 11(4):041104. [PubMed: 16965132]
40. Seo I, You JS, Hayakawa CK, Venugopalan V. Perturbation and differential Monte Carlo methods for measurement of optical properties in a layered epithelial tissue model. J Biomed Opt. 2007; 12(1):014030. [PubMed: 17343505]
41. Pham TH, Eker C, Durkin A, Tromberg BJ, Andersson-Engels S. Quantifying the optical properties and chromophore concentrations of turbid media by chemometric analysis of hyperspectral diffuse reflectance data collected using a Fourier interferometric imaging system. Appl Spectrosc. 2001; 55(8):1035–1045.
42. Tian H, Liu Y, Wang L, Zhang X, Gao Z. Influence of high-order optical parameters of tissue on spatially resolved reflectance in the region close to the source. Chin Opt Lett. 2006; 4(2):105–107.
43. Charvet I, Theuler P, Vermeulen B, Saint-Ghislain M, Biton C, Jacquet J, Bevilacqua F, Depeursinge C, Meda P. A new optical method for the non-invasive detection of minimal tissue alterations. Phys Med Biol. 2002; 47:2095–2108. [PubMed: 12118603]
44. Kienle A, Lilge L, Patterson MS, Hibst R, Steiner R, Wilson BC. Spatially resolved absolute diffuse reflectance measurements for noninvasive determination of the optical scattering and absorption coefficients of biological tissue. Appl Opt. 1996; 35(13):2304–2314. [PubMed: 21085367]

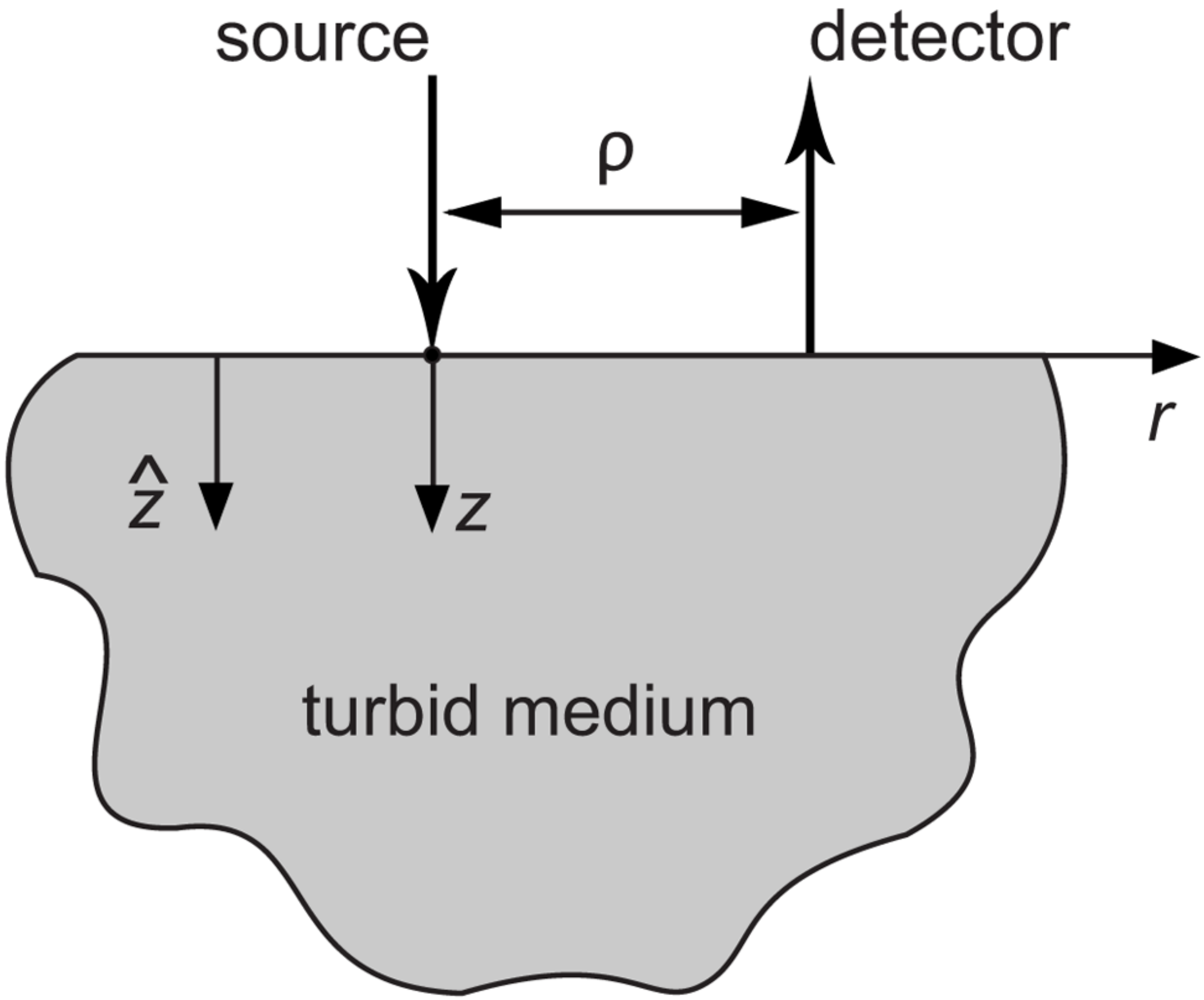

Fig. 1.
Schematic of model geometry.

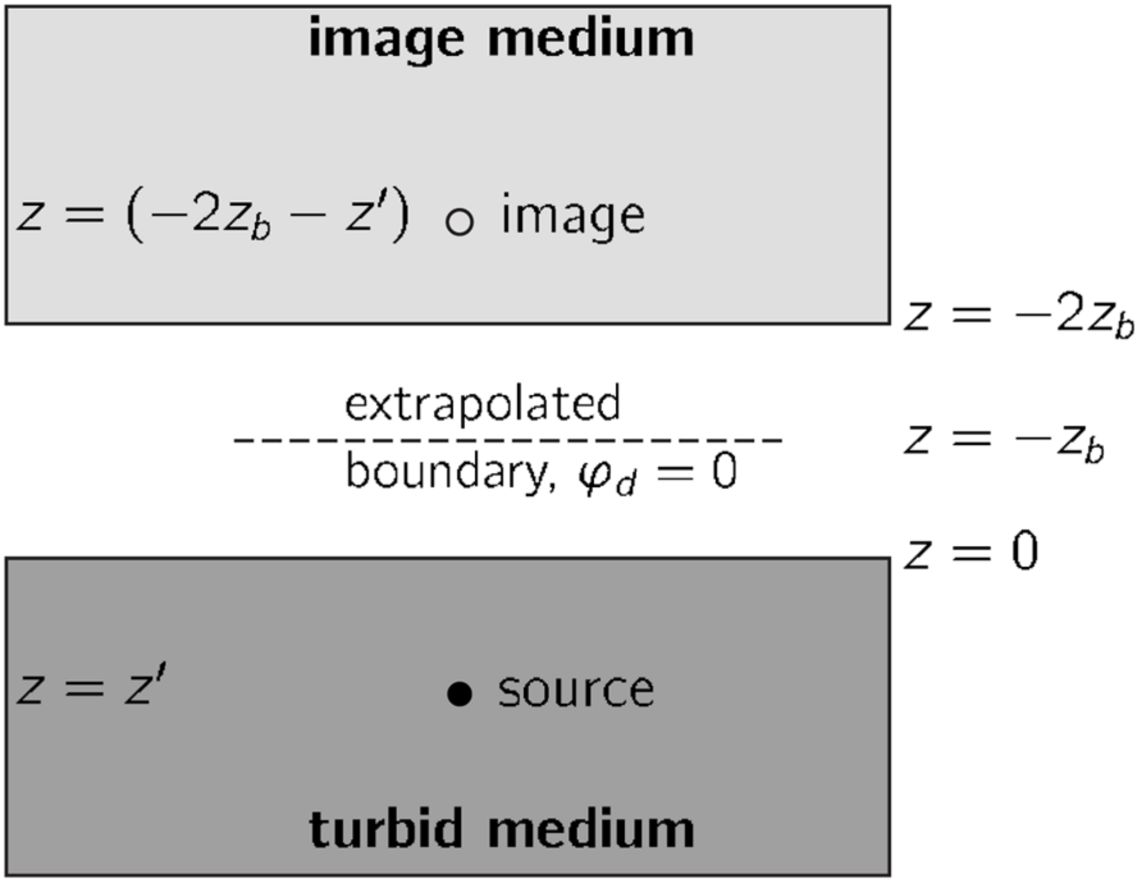

Fig 2.
Source and image configuration for extrapolated boundary condition employed in the δ-P_1 approximation.

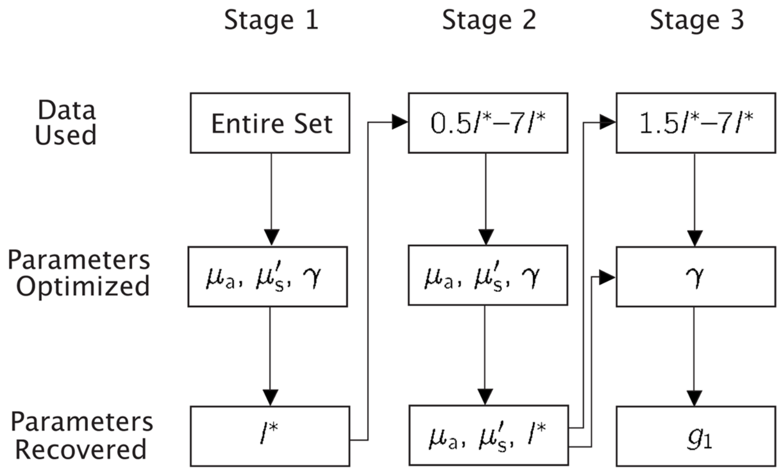

Fig. 3.
Schematic of multi-staged optimization algorithm for determination of optical properties using the δ-P_1 approximation.

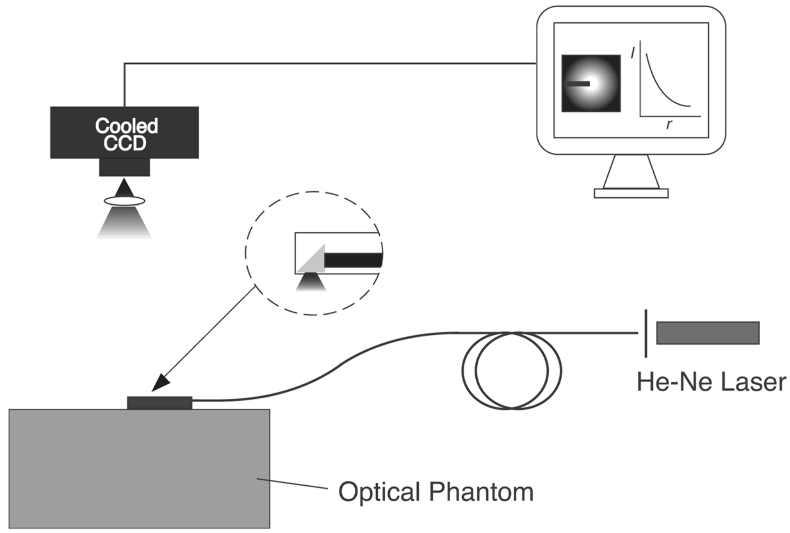

Fig. 4.
Experimental setup for acquisition of spatially resolved diffuse reflectance data.

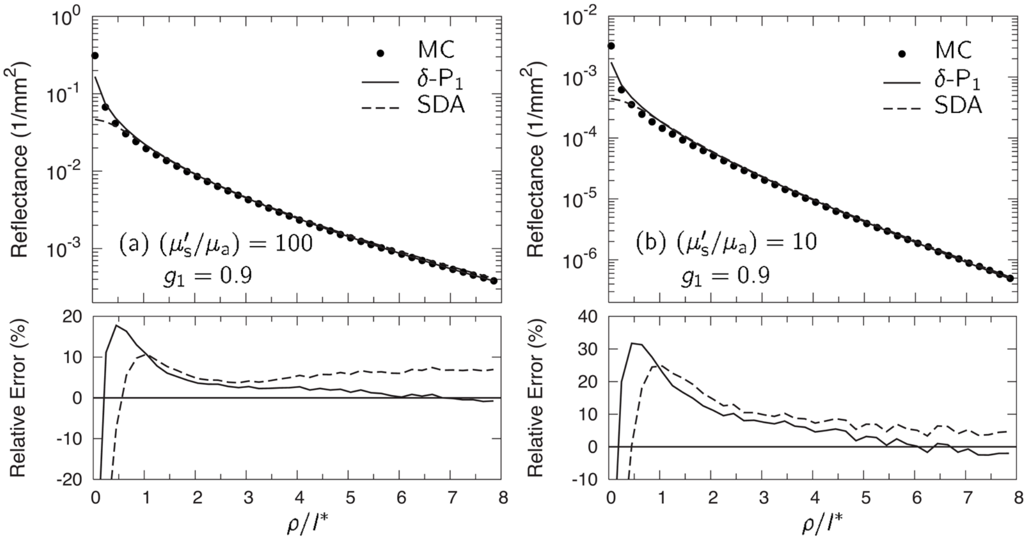

Fig. 5.

Prediction of spatially resolved diffuse reflectance using Monte Carlo (●), δ-P_1 approximation (solid curve), and standard diffusion approximation (dashed curve). The optical coefficients are $n = 1.4$, $\mu_a = 0.01$/mm, (a) (μ_s'/μ_a)=100, $g_1 = 0.9$ and (b) (μ_s'/μ_a)=10, $g_1 = 0.9$. The lower panel of each plot shows the relative error of the δ-P_1 and standard diffusion approximations from the Monte Carlo simulation.

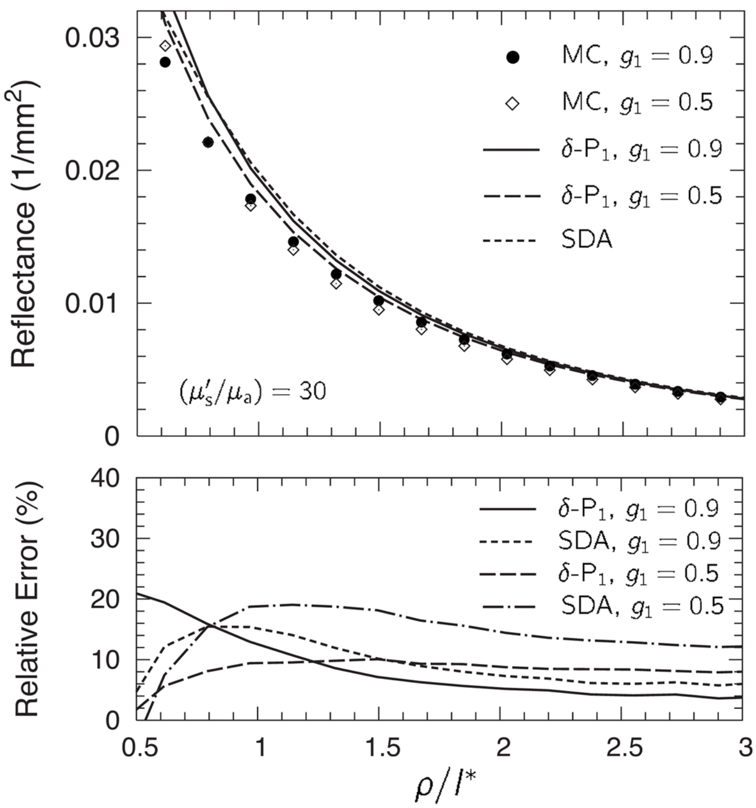

Fig. 6.
Spatially resolved diffuse reflectance as predicted by the δ-P$_1$ approximation (curves) and Monte Carlo simulations (symbols) for pencil beam illumination. Optical properties are μ_a = 0.0344/mm, $\mu_s^{'}$=1.032/mm, $(\mu_s^{'}/\mu_a)$=30, g_1 = 0.9 (solid curve, ●), and 0.5 (dashed curve, ◇). The SRDR prediction from standard diffusion approximation with the same μ_a and $\mu_s^{'}$ is displayed in dotted curve. Lower plot shows the percentage error of the δ-P$_1$ and SDA predictions relative to the Monte Carlo simulations.

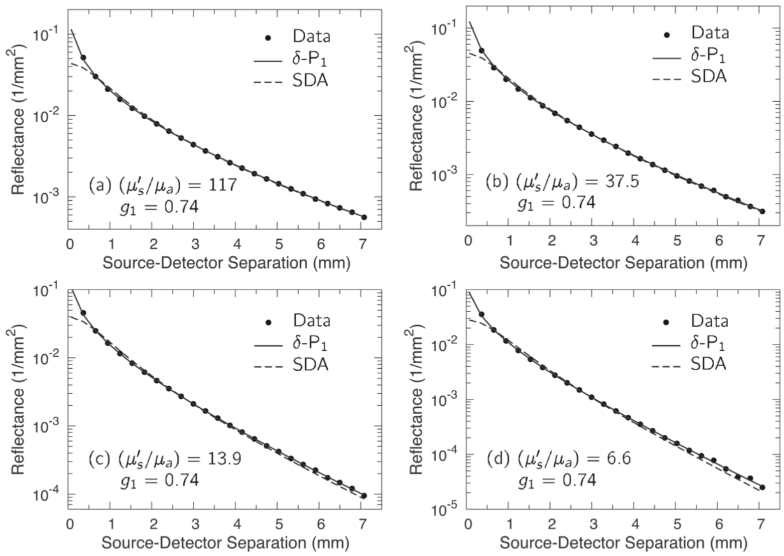

Fig. 7.
Spatially resolved diffuse reflectance measurements (●) from liquid optical phantoms with (a) (μ_s'/μ_a)=117, (b) (μ_s'/μ_a)=37.5, (c) (μ_s'/μ_a)=13.9, and (d) (μ_s'/μ_a)=6.6. Predictions given by the δ-P$_1$ and its recovered optical properties are shown by the solid curves while those given by the SDA and its recovered optical properties are shown by the long dash curves.

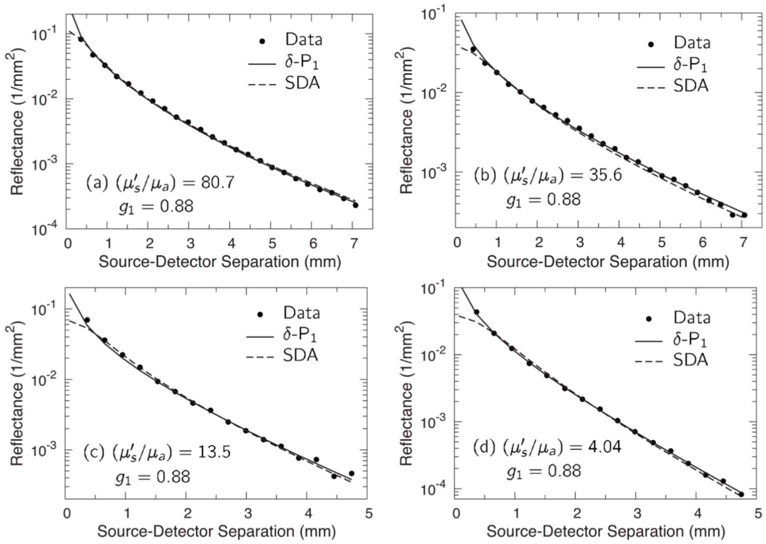

Fig. 8.

Spatially resolved diffuse reflectance measurements (●) from solid optical phantoms with (a) (μ_s'/μ_a)=80.7, (b) (μ_s'/μ_a)=35.6, (c) (μ_s'/μ_a)=13.5, and (d) (μ_s'/μ_a)=4.04. Predictions given by the δ-P_1 and its recovered optical properties are shown by the solid curves while those given by the SDA and its recovered optical properties are shown by the dashed curves.

Table I

Intralipid phantom optical properties and range of s-d separations acquired in the SRDR measurements.

(μ_s'/μ_a)	μ_a (mm^{-1})	μ_s' (mm^{-1})	l^* (mm)	g_1	r_{min} (mm)	r_{max} (mm)
117	7.80×10^{-3}	0.911	1.09	0.74	0.37	7.08
37.5	2.61×10^{-2}	0.978	1.00	0.74	0.37	7.08
13.9	7.04×10^{-2}	0.979	0.95	0.74	0.37	7.08
6.6	1.41×10^{-1}	0.930	0.93	0.74	0.37	7.08

Table II

Siloxane phantom optical properties and range of s-d separations acquired in the SRDR measurements.

(μ_s'/μ_a)	μ_a (mm^{-1})	μ_s' (mm^{-1})	l^* (mm)	g	r_{min} (mm)	r_{max} (mm)
80.7	1.77×10^{-2}	1.428	0.69	0.88	0.37	7.08
35.6	2.92×10^{-2}	1.039	0.94	0.88	0.37	7.08
13.5	9.97×10^{-2}	1.342	0.69	0.88	0.37	4.75
4.04	2.74×10^{-1}	1.107	0.72	0.88	0.37	4.75

Table III

Recovered optical properties after stage 1 of the δ-P_1 approximation-based multi-stage algorithm from SRDR measurements of Intralipid phantoms. Numbers in parenthesis represent relative error in %.

	Stage 1 Result							
Model	(μ_s'/μ_a)		μ_a (mm^{-1})		μ_s' (mm^{-1})		l^* (mm)	
True	117.0	—	7.80×10^{-3}	—	0.911	—	1.09	—
δ-P_1	90.5	(−22.7)	9.74×10^{-3}	(24.9)	0.881	(−3.3)	1.12	(3.2)
True	37.5	—	2.61×10^{-2}	—	0.978	—	1.00	—
δ-P_1	36.2	(−3.6)	2.61×10^{-2}	(0.0)	0.944	(−3.5)	1.03	(3.6)
True	13.9	—	7.04×10^{-2}	—	0.979	—	0.95	—
δ-P_1	10.6	(−23.7)	8.01×10^{-2}	(13.8)	0.850	(−13.2)	1.08	(12.9)
True	6.60	—	1.41×10^{-1}	—	0.930	—	0.93	—
δ-P_1	4.28	(−35.2)	1.68×10^{-1}	(19.6)	0.719	(−22.7)	1.13	(20.7)

Table IV

Final results for Intralipid optical properties as recovered by the δ-P$_1$ approximation-based multi-stage inversion algorithm [δ-P$_1$ (final)] from the SRDR measurements. μ_a and μ_s' are determined by stage 2 while g_1 is determined by stage 3. Optical properties recovered after stage 1 of the δ-P$_1$ approximation-based inversion algorithm [δ-P$_1$ (S1)] and a single-stage SDA-based inversion algorithm [SDA] are also provided for comparison. Numbers in parenthesis represent relative error in %.

Model	(μ_s'/μ_a)		**μ_a (mm^{-1})**		μ_s' (mm^{-1})		***l**(mm)**		**g_1**	
	117.0	—	7.80×10^{-3}	—	0.911	—	1.09	—	0.74	—
δ-P$_1$ (final)	96.4	(−17.4)	9.52×10^{-3}	(22.1)	0.918	(0.8)	1.08	(−1.0)	0.65	(−12.2)
δ-P$_1$ (S1)	90.5	(−22.7)	9.74×10^{-3}	(24.9)	0.881	(−3.3)	1.12	(3.2)	—	
SDA	156.0	(33.2)	6.25×10^{-3}	(−19.9)	0.972	(6.7)	1.02	(−6.1)	—	
	37.5	—	2.61×10^{-2}	—	0.978	—	1.00	—	0.74	—
δ-P$_1$ (final)	36.0	(−4.0)	2.61×10^{-2}	(−0.1)	0.939	(−4.0)	1.04	(4.1)	0.74	(0.3)
δ-P$_1$ (S1)	36.2	(−3.6)	2.61×10^{-2}	(0.0)	0.944	(−3.5)	1.03	(3.6)	—	
SDA	44.3	(18.1)	2.25×10^{-2}	(−13.7)	0.996	(1.8)	0.98	(−1.3)	—	
	13.9	—	7.04×10^{-2}	—	0.979	—	0.95	—	0.74	—
δ-P$_1$ (final)	11.7	(−15.7)	7.67×10^{-2}	(9.0)	0.899	(−8.2)	1.03	(7.6)	0.61	(−16.6)
δ-P$_1$ (S1)	10.6	(−23.7)	8.01×10^{-2}	(13.8)	0.850	(−13.2)	1.08	(12.9)	—	
SDA	11.8	(−15.2)	7.88×10^{-2}	(11.9)	0.929	(−5.1)	0.99	(4.1)	—	
	6.60	—	1.41×10^{-1}	—	0.930	—	0.93	—	0.74	—
δ-P$_1$ (final)	4.80	(−27.2)	1.60×10^{-1}	(14.1)	0.768	(−17.4)	1.07	(15.3)	0.61	(−16.6)
δ-P$_1$ (S1)	4.28	(−35.2)	1.68×10^{-1}	(19.6)	0.719	(−22.7)	1.13	(20.7)	—	
SDA	4.12	(−37.5)	1.81×10^{-1}	(29.0)	0.746	(−19.8)	1.08	(15.5)	—	

Table V

Recovered optical properties after stage 1 of the δ-P$_1$ approximation-based multi-stage algorithm from SRDR measurements of siloxane phantoms. Numbers in parenthesis represent relative error in %.

	Stage 1 Result							
Model	(μ_s'/μ_a)		μ_a (mm^{-1})		μ_s' (mm^{-1})		l^*(mm)	
True	80.7	—	1.77×10^{-2}	—	1.428	—	0.69	—
δ-P$_1$	86.8	(7.6)	1.75×10^{-2}	(−0.8)	1.519	(6.4)	0.65	(−5.9)
True	35.6	—	2.92×10^{-2}	—	1.039	—	0.94	—
δ-P$_1$	30.4	(−14.5)	2.91×10^{-2}	(−0.2)	0.886	(−14.7)	1.09	(16.7)
True	13.5	—	9.97×10^{-2}	—	1.342	—	0.69	—
δ-P$_1$	13.9	(3.1)	8.83×10^{-2}	(−11.4)	1.229	(−8.4)	0.76	(9.4)
True	4.07	—	2.74×10^{-1}	—	1.107	—	0.72	—
δ-P$_1$	3.81	(−6.4)	2.35×10^{-1}	(−14.2)	0.895	(−19.2)	0.88	(22.3)

Table VI

Final results for siloxane optical properties as recovered by the δ-P$_1$ approximation-based multi-stage inversion algorithm [δ-P$_1$ (final)] from the SRDR measurements. μ_a and μ_s' are determined by stage 2 while g_1 is determined by stage 3. Optical properties recovered after stage 1 of the δ-P$_1$ approximation-based inversion algorithm [δ-P$_1$ (S1)] and a single-stage SDA-based, inversion algorithm [SDA] are also provided for comparison. Numbers in parenthesis represent relative error in %.

Model	(μ_s'/μ_a)		μ_a (mm^{-1})		μ_s' (mm^{-1})		l^* (mm)		g_1	
	80.7	—	1.77×10^{-2}	—	1.428	—	0.69	—	0.88	—
δ-P$_1$ (final)	84.9	(5.3)	1.76×10^{-2}	(−0.6)	1.495	(4.7)	0.66	(−4.4)	0.89	(1.6)
δ-P$_1$ (S1)	86.8	(7.6)	1.75×10^{-2}	(−0.8)	1.519	(6.4)	0.65	(−5.9)	—	
SDA	75.1	(−7.0)	2.00×10^{-2}	(13.2)	1.501	(5.1)	0.65	(−5.0)	—	
	35.6	—	2.92×10^{-2}	—	1.039	—	0.94	—	0.88	—
δ-P$_1$ (final)	39.2	(10.3)	2.64×10^{-2}	(−9.5)	1.036	(−0.3)	0.94	(0.6)	0.76	(−13.6)
δ-P$_1$ (S1)	30.4	(−14.5)	2.91×10^{-2}	(−0.2)	0.886	(−14.7)	1.09	(16.7)	—	
SDA	28.3	(−20.6)	3.16×10^{-2}	(8.3)	0.893	(−14.1)	1.08	(15.6)	—	
	13.5	—	9.97×10^{-2}	—	1.342	—	0.69	—	0.88	—
δ-P$_1$ (final)	13.9	(3.4)	8.83×10^{-2}	(−11.4)	1.229	(−8.4)	0.76	(9.4)	0.79	(−10.3)
δ-P$_1$ (S1)	13.9	(3.1)	8.83×10^{-2}	(−11.4)	1.229	(−8.4)	0.76	(9.4)	—	
SDA	19.6	(45.2)	7.15×10^{-2}	(−28.3)	1.398	(4.2)	0.68	(−1.9)	—	
	4.07	—	2.74×10^{-1}	—	1.107	—	0.72	—	0.88	—
δ-P$_1$ (final)	4.02	(−1.0)	2.27×10^{-1}	(−17.1)	0.913	(−17.6)	0.88	(21.2)	0.73	(−16.8)
δ-P$_1$ (S1)	3.81	(−6.4)	2.35×10^{-1}	(−14.2)	0.895	(−19.2)	0.88	(22.3)	—	
SDA	3.25	(−19.5)	2.54×10^{-1}	(−7.3)	0.826	(−25.4)	0.93	(27.9)	—	